



Contents lists available at ScienceDirect

Acta Biomaterialia

journal homepage: www.elsevier.com/locate/actbio

Full length article

Unraveling the influence of channel size and shape in 3D printed ceramic scaffolds on osteogenesis



Ali Entezari^{a,b,1}, Qianju Wu^{c,d,1}, Mohammad Mirkhalaf^{e,f,g}, Zufu Lu^b, Iman Roohani^b, Qing Li^h, Colin R. Dunstan^b, Xinquan Jiang^{c,*}, Hala Zreiqat^{b,*}

^a School of Biomedical Engineering, Faculty of Engineering and Information Technology, University of Technology Sydney, NSW 2007, Australia

^b Tissue Engineering and Biomaterials Research Unit, School of Biomedical Engineering, The University of Sydney, NSW 2006, Australia

^c Department of Prosthodontics, Oral Bioengineering, and Regenerative Medicine Lab, Ninth People's Hospital, Shanghai Jiao Tong University, Shanghai 200011, China

^d Stomatological Hospital of Xiamen Medical College, Xiamen Key Laboratory of Stomatological Disease Diagnosis and Treatment, Xiamen, Fujian, China

^e School of Mechanical, Medical and Process Engineering, Queensland University of Technology, 2 George St Brisbane, QLD 4000, Australia

^f Centre for Biomedical Technologies, Queensland University of Technology (QUT), Brisbane, QLD 4059, Australia

^g Centre for Materials Science, Queensland University of Technology (QUT), Brisbane, QLD 4000, Australia

^h School of Aerospace, Mechanical and Mechatronic Engineering, The University of Sydney, Sydney, NSW 2006, Australia

ARTICLE INFO

Article history:

Received 6 December 2023

Revised 31 March 2024

Accepted 11 April 2024

Available online 18 April 2024

Keywords:

Bone scaffolds

Bioceramics

3D printing

Tissue engineering

Scaffold architecture

ABSTRACT

Bone has the capacity to regenerate itself for relatively small defects; however, this regenerative capacity is diminished in critical-size bone defects. The development of synthetic materials has risen as a distinct strategy to address this challenge. Effective synthetic materials to have emerged in recent years are bioceramic implants, which are biocompatible and highly bioactive. Yet nothing suitable for the repair of large bone defects has made the transition from laboratory to clinic. The clinical success of bioceramics has been shown to depend not only on the scaffold's intrinsic material properties but also on its internal porous geometry. This study aimed to systematically explore the implications of varying channel size, shape, and curvature in tissue scaffolds on *in vivo* bone regeneration outcomes. 3D printed bioceramic scaffolds with varying channel sizes (0.3 mm to 1.5 mm), shapes (circular vs rectangular), and curvatures (concave vs convex) were implanted in rabbit femoral defects for 8 weeks, followed by histological evaluation. We demonstrated that circular channel sizes of around 0.9 mm diameter significantly enhanced bone formation, compared to channel with diameters of 0.3 mm and 1.5 mm. Interestingly, varying channel shapes (rectangular vs circular) had no significant effect on the volume of newly formed bone. Furthermore, the present study systematically demonstrated the beneficial effect of concave surfaces on bone tissue growth *in vivo*, reinforcing previous *in silico* and *in vitro* findings. This study demonstrates that optimizing architectural configurations within ceramic scaffolds is crucial in enhancing bone regeneration outcomes.

Statement of significance

Despite the explosion of work on developing synthetic scaffolds to repair bone defects, the amount of new bone formed by scaffolds *in vivo* remains suboptimal. Recent studies have illuminated the pivotal role of scaffolds' internal architecture in osteogenesis. However, these investigations have mostly remained confined to *in silico* and *in vitro* experiments. Among the *in vivo* studies conducted, there has been a lack of systematic analysis of individual architectural features. Herein, we utilized bioceramic 3D printing to conduct a systematic exploration of the effects of channel size, shape, and curvature on bone formation *in vivo*. Our results demonstrate the significant influence of channel size and curvature on *in vivo* outcomes. These findings provide invaluable insights into the design of more effective bone scaffolds.

© 2024 The Authors. Published by Elsevier Ltd on behalf of Acta Materialia Inc.

This is an open access article under the CC BY license (<http://creativecommons.org/licenses/by/4.0/>)

* Corresponding authors.

E-mail addresses: xinquanjiang@aliyun.com (X. Jiang), hala.zreiqat@sydney.edu.au (H. Zreiqat).

¹ These others contributed equally.

1. Introduction

The effective management of bone loss due to trauma, cancer, and other diseases is a major clinical challenge in orthopedics surgery [1]. Current clinical gold standards for treating bone defects primarily include autografts and allografts. However, these treatment strategies often face challenges in providing satisfactory bone regeneration outcomes, such as donor site morbidity, infection, and disease transmission [2]. A viable alternative that has been attracting growing interest in recent years is bone tissue engineering, in which synthetic bone substitutes composed of porous metals, polymers, or bioceramics are provided as tissue scaffolds to reconstruct bone defects and restore the functionality of normal bone tissue [3].

Over the past few decades, significant efforts have been devoted to developing synthetic bone tissue scaffolds [4]. Yet, despite significant advances in the field, current tissue scaffolds are ineffective in treating large bone defects and have rarely been translated to the clinic [5,6]. One of the main challenges in the clinical translation of these bone substitutes has been their suboptimal bone regeneration outcome compared with the current clinical gold standards – *i.e.*, autografts and allografts. In tissue engineering, factors such as material properties, pore architecture, surface properties, and biophysical stimuli influence bone tissue formation within scaffolds [7–13]. Among these, the internal architecture of the scaffolds has been identified as a critical determinant of osteogenesis [14–16].

Recent *in vitro* and *in vivo* studies have shed light on the critical role of scaffolds' internal architecture – such as their porosity, interconnectivity, pore size, and shape – in osteogenesis [14,17–19]. Amongst various architectural features, the effects of porosity and interconnectivity have been most explored. Scaffolds with 100 % pore interconnectivity are shown to significantly improve bone tissue formation compared with those with disconnected pores [20,21]. Furthermore, scaffolds with higher porosity (*i.e.*, lower solid volume) are known to enhance bone tissue regeneration, however, increased porosity is usually associated with mechanically less strong scaffolds [22].

On length scales exceeding that of an individual cell, typically in the range of hundreds of microns to millimetres, geometric parameters such as pore size, shape, and curvature play a pivotal role in dictating cell organization and tissue patterning [10,23,24]. Pores can have various shapes – *e.g.*, circular or rectangular – affecting the bone formation process within the scaffolds. For example, Bidan et al. [23] showed that the initial tissue deposition in cross-shaped pores was significantly faster than that observed in square pores *in vitro*. The curvature of a pore could also affect bone tissue formation. *In vitro* and *in silico* studies have shown that the rate of local tissue growth is directly proportional to the mean surface curvature, with an accelerated growth rate observed on concave surfaces with a high mean curvature [25]. Another macroscopic geometric consideration is pore size, where empirical studies consistently indicate its pronounced influence on outcomes of bone tissue formation [26], with a predominant recommendation favouring sizes beyond 300 μm [11]. Nevertheless, the exclusive role of pore size in bone tissue formation remains largely unknown due to the lack of systematic *in vivo* analyses.

Studies exploring the effects of pore size, shape, and curvature are mostly carried out within *in vitro* settings, which fail to replicate the mechano-biological environment of the living body. Of those that have explored pore size and shape *in vivo* [27], there is a lack of a systematic approach to exclusively determine the sole effects of pore size, shape, and curvature on *in vivo* osteogenesis.

Indeed, architectural features of scaffolds are often interrelated, and altering one structural parameter can have a cascading effect on the other geometric features within the scaffold. For example,

when pore size is increased, it usually leads to an elevation in the porosity of the scaffold, thereby hindering the ability to isolate the impact of pore size alone. This interaction can make it challenging to isolate the impact of a single parameter, such as pore size on bone formation outcomes in the scaffold.

In the present study, we used a systematic approach to isolate and understand the specific effects of pore size, shape, and curvature in 3D printed bioceramic scaffolds, on *in vivo* bone tissue regeneration. To be able to differentiate the effect of pore size and shape from other architectural properties of the scaffolds, we created scaffolds with isolated channels of various sizes, shapes, and curvatures. The use of channels instead of traditional pores allowed for a more controlled investigation of each geometric feature's individual impact on bone formation, minimizing confounding influences from interconnected pore networks. Scaffolds were fabricated from Baghdadite ($\text{Ca}_3\text{ZrSi}_2\text{O}_9$), a bioactive bioceramic material with properties that support osteoconduction [28], using our recently developed ceramic stereolithography (SLA) 3D printing procedure [28,29]. This method is essential for precisely controlling the scaffold's architectural features, including channel size and shape. The baghdadite scaffolds were implanted in a cylindrical defect in the rabbit femoral shaft near the femoral head for 8 weeks to determine the volume of bone ingrowth in each channel within the implants.

2. Materials and methods

2.1. Scaffold design

To systematically investigate the effects of channel size, shape, and curvature on bone tissue formation, we designed bioceramic scaffolds in the shape of cylindrical bone plugs in SolidWorks. These scaffolds had an overall diameter and depth of 7 mm and 3.2 mm, respectively. Table 1 depicts the geometric details of various channel sizes, shapes, and curvatures explored in the current study. The circular channels had five different diameters: 0.3 mm, 0.6 mm, 0.9 mm, 1.2 mm, and 1.5 mm. The rectangular channels were designed either to have a similar surface area to circular channels with diameters of 0.6 mm and 0.9 mm or to allow circles with diameters of 0.6 mm and 0.9 mm to fit into them. The curved surfaces were either concave or convex with diameters of 0.3 mm, 0.6 mm, and 0.9 mm.

2.2. Scaffolds fabrication

The scaffolds were first designed in SolidWorks and then converted to STL files. The 3D printing of the scaffolds was done by following our recently developed ceramic 3D printing procedure [28,29]. In short, baghdadite was synthesized using solid-state synthesis. The precursors were calcium oxide CaO, zirconium oxide ZrO_2 , and silicon oxide SiO_2 , all sourced from Sigma Aldrich (Australia). Ball milling (Retsch PM 400, Germany) at 200 rpm for three hours was used to ensure a homogenized particle size across all precursors, measured using laser scattering particle size analysis (Horiba, Japan). The refined slurry was formed into pellets using uniaxial dry pressing. The pellets were then fired at 1300 °C for three hours for the reaction between the precursors to complete. The sintered pellets were ground using ball milling to make the baghdadite particles. 62 % of these particles were mixed with 19 % photosensitive polymer (clear resin V4, Formlabs, USA) and 19 % dispersant (Twin 20, Sigma Aldrich) using ball milling at 100 rpm for 30 min to make the ceramics resin. Formlabs Form 2 printer (NY, US) was then used to print the scaffolds that were designed by Solidworks (MA, US). The baghdadite synthesis, resin development, and sintering details are reported in [28,29].

Table 1
Geometric details of various channel sizes, shapes, and curvatures explored in the current study.

Diameter (mm)	Circular channels					
	0.3	0.6	0.9	1.2	1.5	
	Rectangular channels					
	For comparison with circular channels with diameter of 0.6 mm			For comparison with circular channels with diameter of 0.9 mm		
Length (mm)	0.51	0.6	0.3	0.79	0.9	0.6
width (mm)	0.51	0.6	0.85	0.79	0.9	1.05
	Curved surfaces					
	Concave			Convex		
Diameter (mm)	0.3	0.6	0.9	0.3	0.6	0.9

To ensure consistency in the cleaning of the samples, we followed a standardized protocol as follows: After removing the parts from the 3D printer, the samples were immersed in isopropyl alcohol (IPA) for 30 min to remove the uncured material from the channels. To further ensure the complete removal of uncured material, we subjected the samples to ultrasonication for 5 min in an IPA bath. After sintering, we used high-pressure air to remove any dust and debris from the samples. The samples were then rinsed with distilled water to wash off any remaining dust and debris. Following these cleaning steps, the samples were transferred to a clean container for storage and sterilization before surgery.

2.3. Micro-CT scanning

To evaluate the quality and accuracy of the scaffolds' internal architecture, representative samples were scanned post-3D printing. μ CT-based models were then created from the μ -CT images of these specimens. For this purpose, each scaffold was scanned using a SkyScan 1172 (Kontich, Belgium) at an 8 μ m voxel size resolution with 100 kV, 100 μ A, and a 1.0 mm aluminum filter. Projection images were integrated for 885 ms every 0.5° over a full 180° rotation. Each raw data set was then reconstructed into an axial stack saved as greyscale BMP images using SkyScan's reconstruction software NRecon (Kontich, Belgium) for further processing. Reconstruction parameters were kept constant for each scan of a specimen to provide consistent greyscale factors for the analysis. Each set of reconstructed images was then imported into the image-processing software ScanIP (Simpleware Ltd, Exeter, UK). Furthermore, we conducted μ -CT scanning on the scaffold-bone constructs after harvesting the explants. For these scans, we utilized a SkyScan 1176 μ -CT (Kontich, Belgium) and scanned the explants at an 18 μ m voxel size resolution. It is noted that μ -CT scanning was performed on only 3 of the scaffolds containing circular channels.

2.4. Animal surgical procedures

Mature male rabbits (12 weeks old) were employed for present study. The animal study was reviewed and approved by the Institutional Animal Care and Use Committee of the Ninth People's Hospital, Shanghai Jiao Tong University (SH9H2020-A116-1). The experimental operations were performed in sterile conditions. Briefly, after general anesthesia, an incision along each femoral shaft was made to expose the femur. Then, cylindrical bone defects (~7 mm in diameter and ~3.2 mm in depth) were created by a customized bur in the middle of the epiphysis. Subsequently, each scaffold under strict sterilization was used to restore the defects, and the incision was sutured in layers. Antibiotics were injected post-surgically to prevent inflammation and infection [30]. After the 8-week study

period, the animals were humanely euthanized, and the scaffolds were explanted for further analysis using micro-CT scanning and histological analyses.

In this study, six rabbits were used, with each animal receiving two implants—one in each leg. Due to the death of one rabbit, two samples were lost, resulting in a total of four samples for scaffolds containing circular channels, four samples for scaffolds containing rectangular channels, and two samples for scaffolds containing curved surfaces. Since each scaffold contained at least two repetitions of each specific channel, the sample number for each specific channel was at least twice the number of scaffolds containing that channel. For example, we had four scaffolds containing circular channels, and each scaffold contained two repetitions of circular channels with a diameter of 1.5 mm. Therefore, the sample number for the circular channels with a diameter of 1.5 mm was eight. The specific sample number for each channel is detailed in the captions of the relevant figures.

2.5. Histological observation

At 8 weeks, explants of scaffolds were excised and left undecalcified for histological evaluation. The specimens were embedded in PMMA and trimmed into 10- μ m-thick slices using a microtome (Leica, Germany). Then, at least two transversal cross-sections (one for Toluidine Blue staining and one for Van Gieson's picrofuchsin staining) parallel to the top and bottom surfaces of the cylindrical scaffolds were cut approximately in the middle of the scaffolds, approximately 1.6 mm away from the cancellous bone. The sections, with a thickness of ~10 μ m, were subsequently stained with Toluidine Blue or Van Gieson's picrofuchsin as previously described in [17,31].

2.6. Statistical analysis

The statistical analysis was performed using GraphPad Prism v1.0 (GraphPad, San Diego, California, USA). Data are represented as mean (SD). For the statistical analyses, ANOVA followed by Tukey's multiple comparisons test was used. A calculated *p*-value of less than 0.05 was considered statistically significant.

3. Results

3.1. Circular channels with varying dimensions

To systematically investigate the effects of channel size on bone tissue formation, we designed and 3D printed scaffolds with isolated circular channels with diameters ranging from ~0.3 mm to ~1.5 mm (Fig. 1. a and b). These channels, running along the length of the scaffold, were about 3.2 mm long and open on both

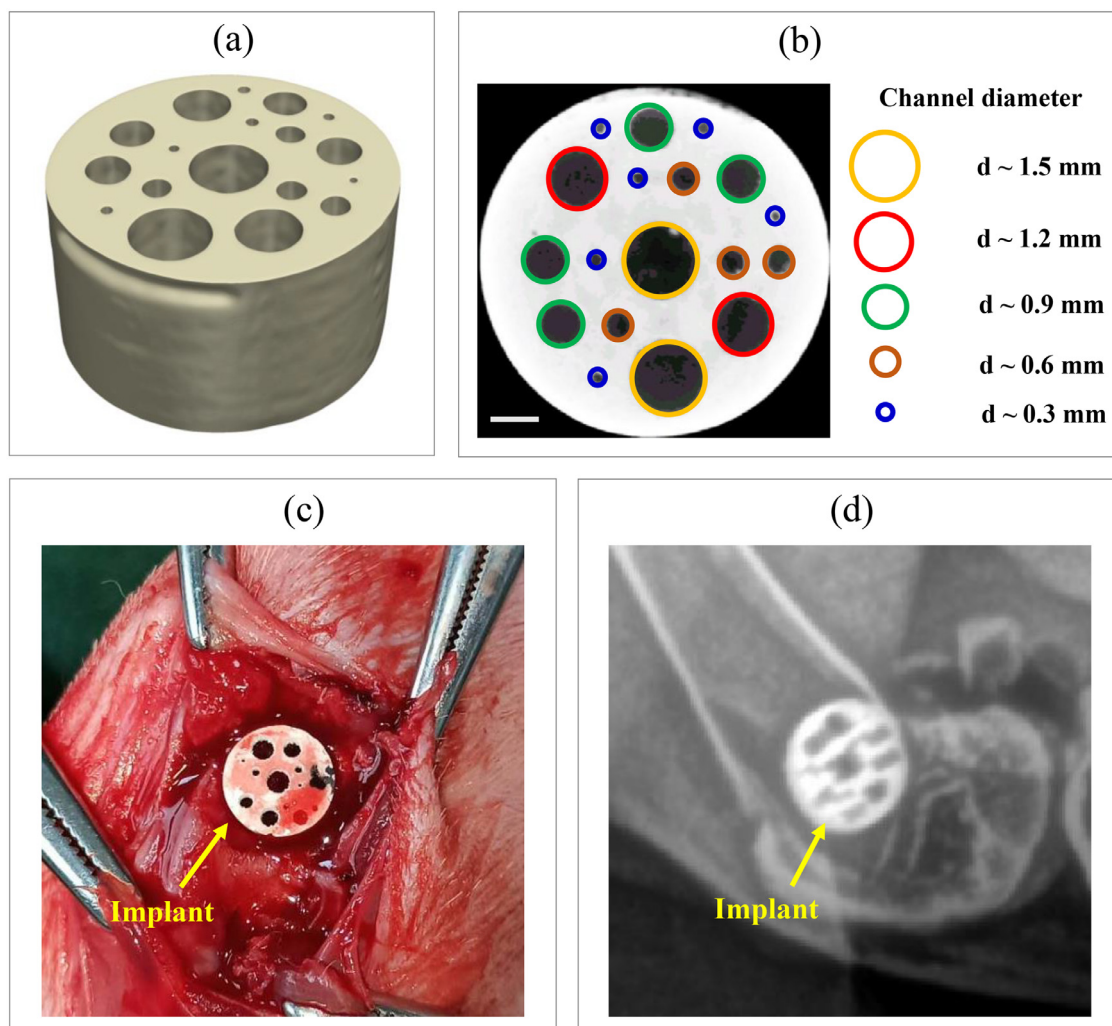


Fig. 1. Scaffolds containing isolated circular channels with varying diameters. (a) The 3D model of the scaffold reconstructed from μ -CT images; (b) the top surface of the scaffold depicting the random distribution of the channels with varying diameters; (c) the scaffold implanted in the defect; (d) post-operative x-ray image of the defect site. Scale bar = 1 mm.

the bottom and top sides of the scaffolds. The bottom side was exposed to the cancellous bone, and the top side was exposed to the periosteum, in order to ensure that the scaffolds are in direct contact with the surrounding bone tissue.

Each scaffold contained at least two replicates of each specific channel size positioned randomly in the construct. If a channel could not be cleaned thoroughly and consequently blocked during the fabrication and cleaning process, it was excluded from the data analyses. The scaffolds had an overall diameter and depth of 7 mm and 3.2 mm, respectively. They were press-fitted into bone defects of the same dimensions located in the rabbit femoral shaft near the femoral head (Fig. 1. c and d).

Fig. 2 depicts representative images of the histological sections for each specific channel size. The bone formed in each channel appeared of normal structure with numerous osteocytes and mixed woven and mature lamellar bone. Histological results also revealed occasional deposits of adipose tissue. There were sections of the bone surface that show crenated surfaces (indicated by arrows) on the ingrowing new bone indicating remodeling activity is occurring.

Fig. 3a compares the percentages of newly formed bone area (*i.e.*, area of new bone tissue relative to the total area of the channel) for each of the five different channel sizes. These newly formed bone areas were calculated in the same transversal cross-

section located approximately in the middle of the scaffold and running parallel to its top and bottom surfaces. The results showed that bone formed in the channels with a diameter of 0.9 mm had an average percentage growth rate that was 89 % and 94 % higher, compared to channels with diameters of 0.3 mm and 1.5 mm, respectively. While the average bone growth in channels with diameters of 0.6 mm and 1.2 mm was 11 % and 28 % lower, respectively, compared to the bone formation in the channels with a diameter of 0.9 mm, there were no significant differences between the growth rates of bone in the 0.6 mm, 0.9 mm, and 1.2 mm channels.

To verify that the histology results in 2D accurately reflect the actual bone formation volume in 3D channels, new bone tissue volume was quantified in each circular channel using μ -CT analyses, as depicted in Fig. 3b. While the ratio of new bone volume to available volume in each channel (measured using micro-CT analysis) was relatively lower than the ratio of new bone surface area to available surface area in each 2D channel (measured using histology analysis), the trends observed in both analyses were consistent.

To evaluate the ingrowth depth of new bone tissue within each channel, micro-CT data was used to quantify the bone tissue surface area at three distinct depths in each circular channel. The results of this analysis are illustrated in Fig. 4. The micro-CT data

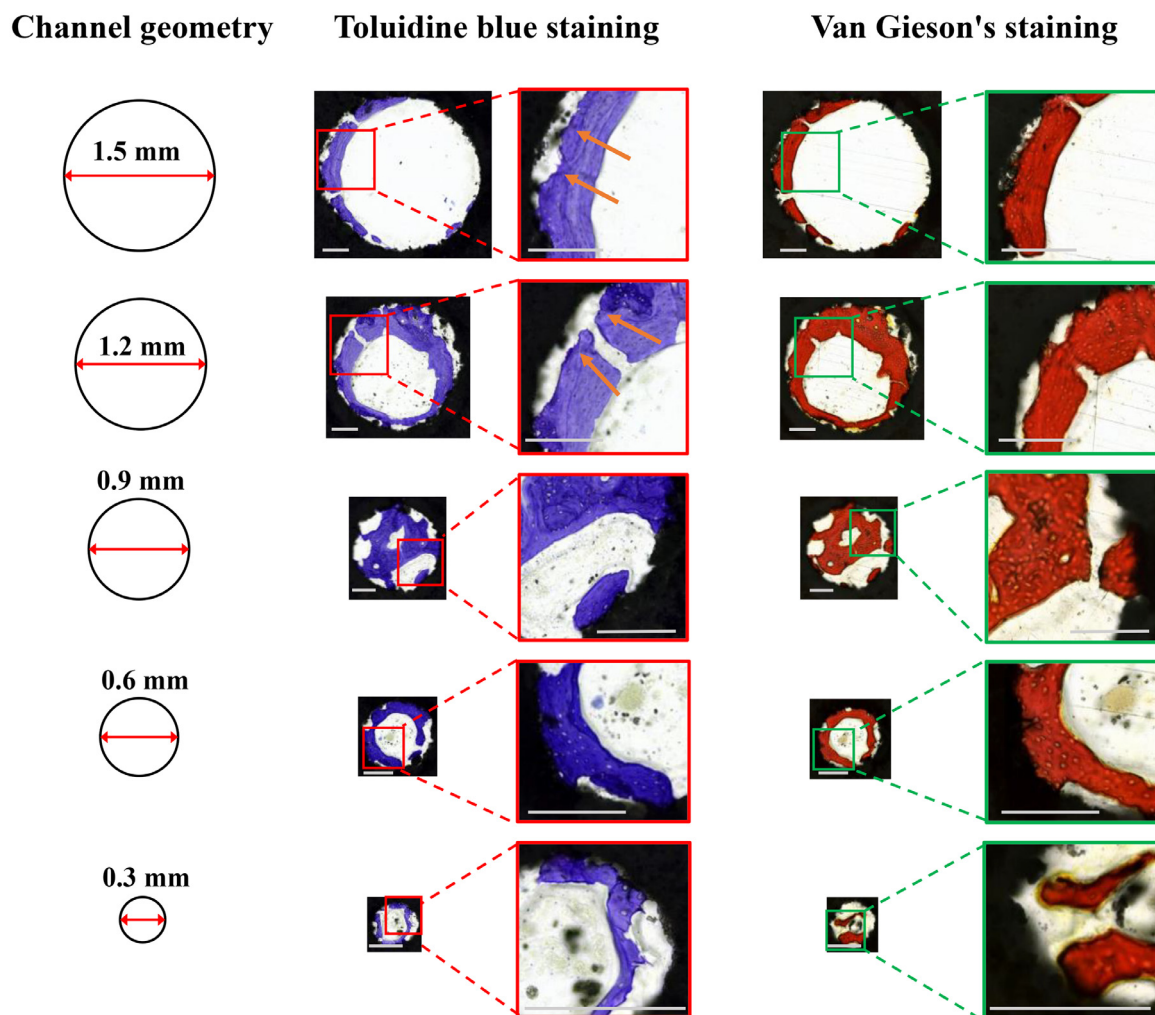


Fig. 2. Representative histology images of circular channels with varying diameters at 8 weeks. The Toluidine Blue staining (black: implant; blue: bone) and Van Gieson's staining (black: implant; red: bone) were used to quantify the newly formed bone in channels at a cross-sections located approximately in the middle of the implant. Scale bar = 0.25 mm.

revealed that bone formation occurred at varying depths in most channels, albeit with differing quantities of new bone tissue at each depth. Notably, we observed a trend of decreasing bone tissue quantity with increasing depth in channels with diameters of 0.3 mm, 0.9 mm, 1.2 mm, and 1.5 mm. Despite this trend, there was no significant difference in bone formation outcomes across these three depths.

3.2. Rectangular channels with varying dimensions and aspect ratios

To investigate how channel shape can affect bone tissue formation *in vivo*, we designed and 3D printed scaffolds containing rectangular channels with varying dimensions and aspect ratios (Fig. 5). Similar to scaffolds with circular channel described in Section 3.1, these scaffolds had overall diameter and depth of 7 mm and 3.2 mm, respectively and were implanted into bone defects of the same dimensions located in the rabbit femoral shaft near the femoral head (Fig. 5. a and b).

In order to establish a meaningful comparison between circular and rectangular channels, we meticulously ensured that both possessed identical channel size during the design process. For this purpose, we considered two different definitions for the channel size when the shape was rectangle: (1) channel size defined as the diameter of the largest circle that can fit inside the rectangle

(Group A2 and B2 in Fig. 5. f); and (2) channel size defined as the diameter of a circle that has the same surface area as that of a rectangle (Group A3, A4, B3, and B4 in Fig. 5. f). We also considered that the rectangle can have any aspect ratio as in Groups A4 and B4 (*i.e.*, a and b can have different dimensions). These longitudinal rectangular channels corresponded to circular channels with diameters of 0.6 mm (Group B1) and 0.9 mm (Group A1) and were randomly positioned within the scaffolds (Fig. 5. e).

Representative histological images for each specific rectangular channel are depicted in Fig. 6. Fig. 7 compares the bone area formed in these six rectangular channels with their corresponding circular channels. These new bone areas were calculated in the same cross-sections running parallel to the top and bottom surfaces of the scaffolds. Quantitative results demonstrated no significant difference between bone growth in the rectangular channels and their corresponding circular channels with diameters of 0.6 mm and 0.9 mm. Moreover, results indicated that changing the aspect ratio (*i.e.*, a/b ratio) of rectangular channels does not change their bone formation rate if their surface areas are consistent.

3.3. Comparison of concave and convex surfaces

To determine how surface convexity/concavity affects osteogenesis, we designed and fabricated a scaffold with concave (negative

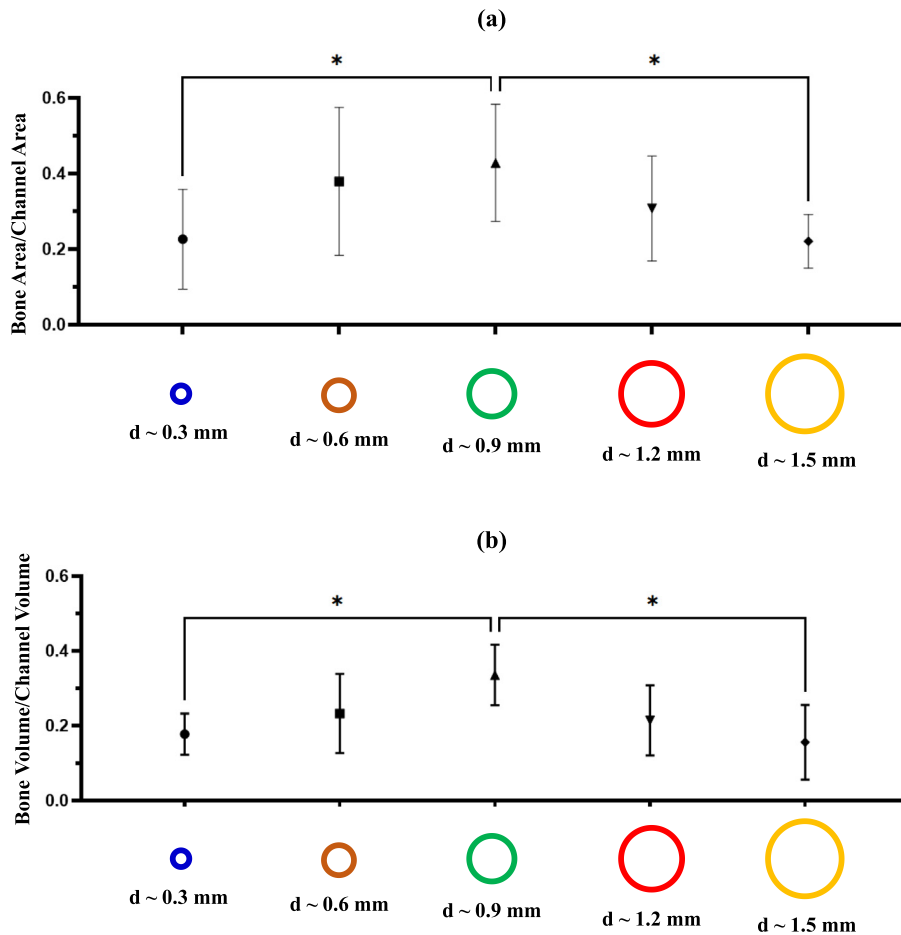


Fig. 3. Quantitative bone formation results of the circular channels. (a) The ratios of the new bone area to the total channel area were measured at histological cross-sections (Van Gieson’s staining) located in the middle of the samples. Bone surface area was measured in the channels with diameters of 0.3 mm ($n = 10$), 0.6 mm ($n = 8$), 0.9 mm ($n = 8$), 1.2 mm ($n = 8$), and 1.5 mm ($n = 8$). (b) The ratios of the new bone volume to the total channel volume were measured using μ -CT data. Bone volume was measured for the channels with diameters of 0.3 mm ($n = 7$), 0.6 mm ($n = 6$), 0.9 mm ($n = 6$), 1.2 mm ($n = 6$), and 1.5 mm ($n = 6$).

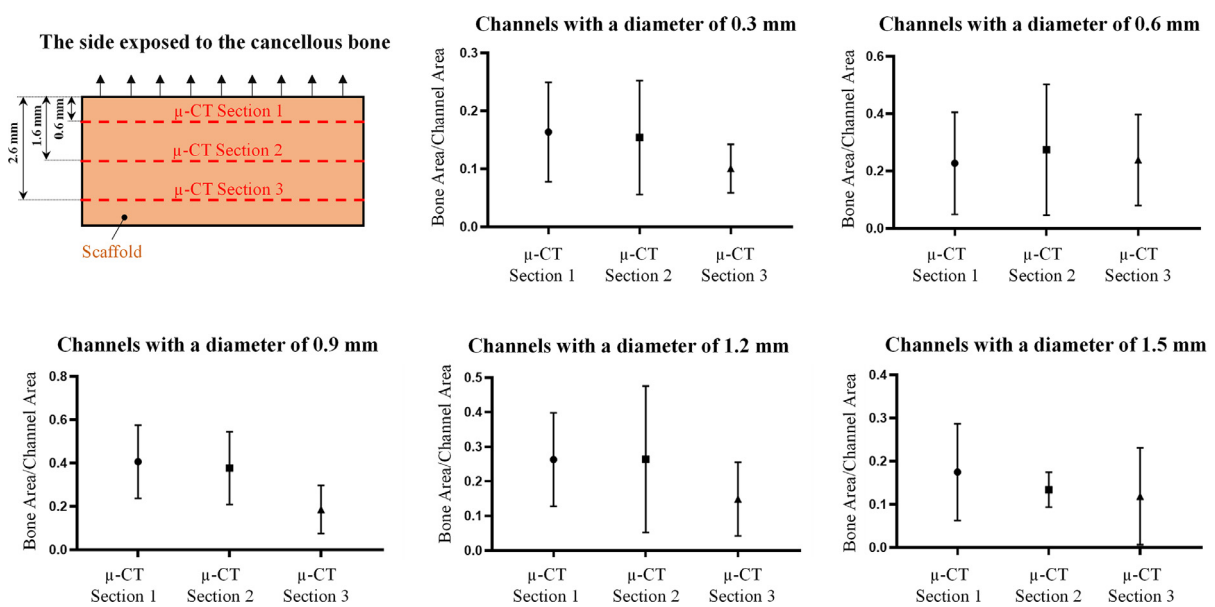


Fig. 4. Comparison of bone formation results at different depths within the circular channels. The μ -CT data were used to measure bone formation (bone area/channel area) at three different depths: 0.6 mm, 1.6 mm, and 2.6 mm away from the cancellous bone. These measurements were taken for circular channels with diameters of 0.3 mm ($n = 7$), 0.6 mm ($n = 6$), 0.9 mm ($n = 6$), 1.2 mm ($n = 6$), and 1.5 mm ($n = 6$).

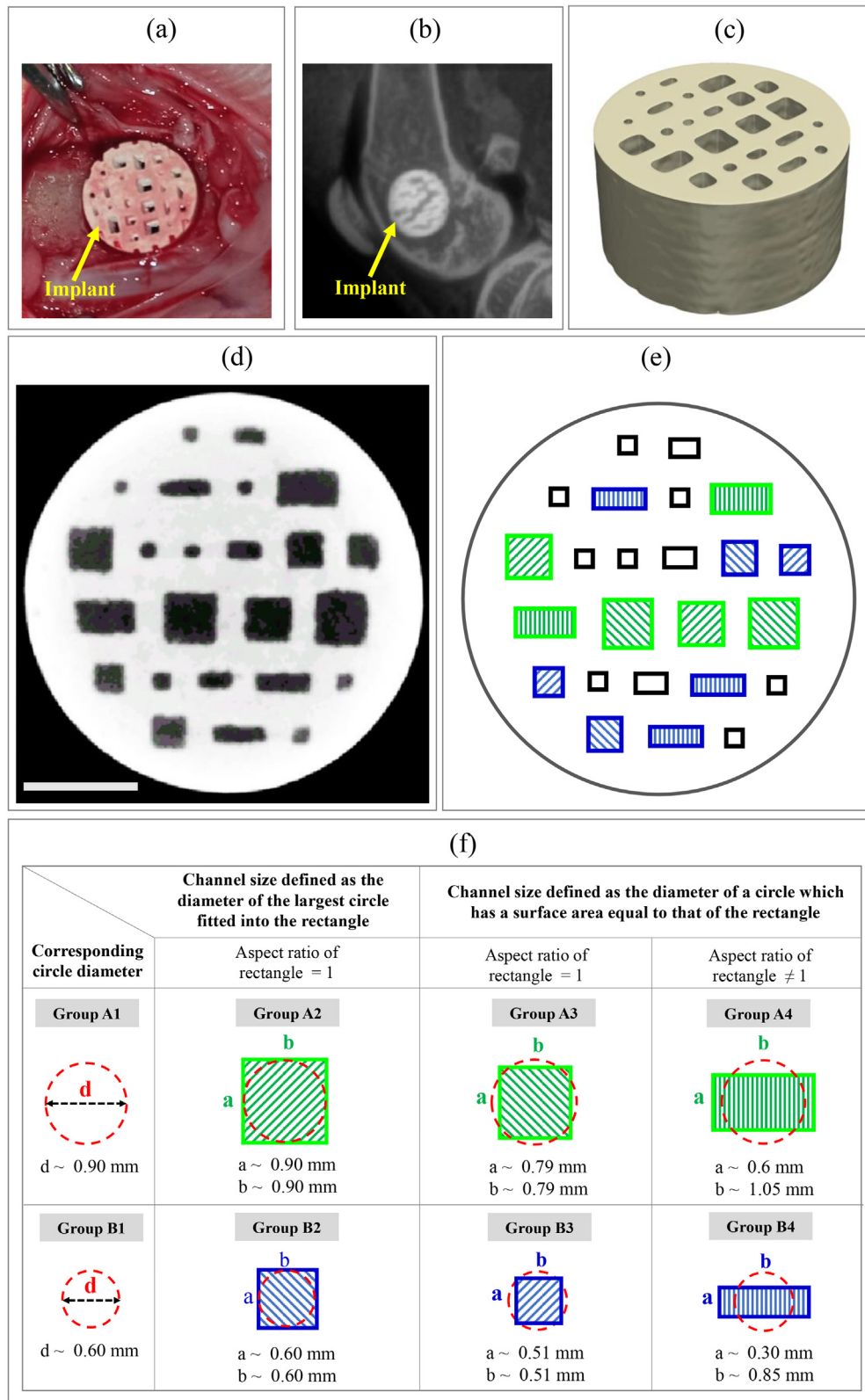


Fig. 5. Geometric and surgical details of scaffolds containing isolated rectangular channels. (a) an image showing the implantation site in a rabbit femur; (b) a post-operative x-ray image of the surgical site; (c) a 3D reconstructed μ -CT model of a scaffold containing rectangular channels before implantation; (d) a cross-sectional μ -CT scan of the scaffold depicting the random distribution of rectangular channels with various dimensions and aspect ratios. This cross-section is perpendicular to the longitudinal direction of the channels; (e) and (f) show the dimensions and distribution of rectangular channels in the scaffold. Scale bar = 2 mm.

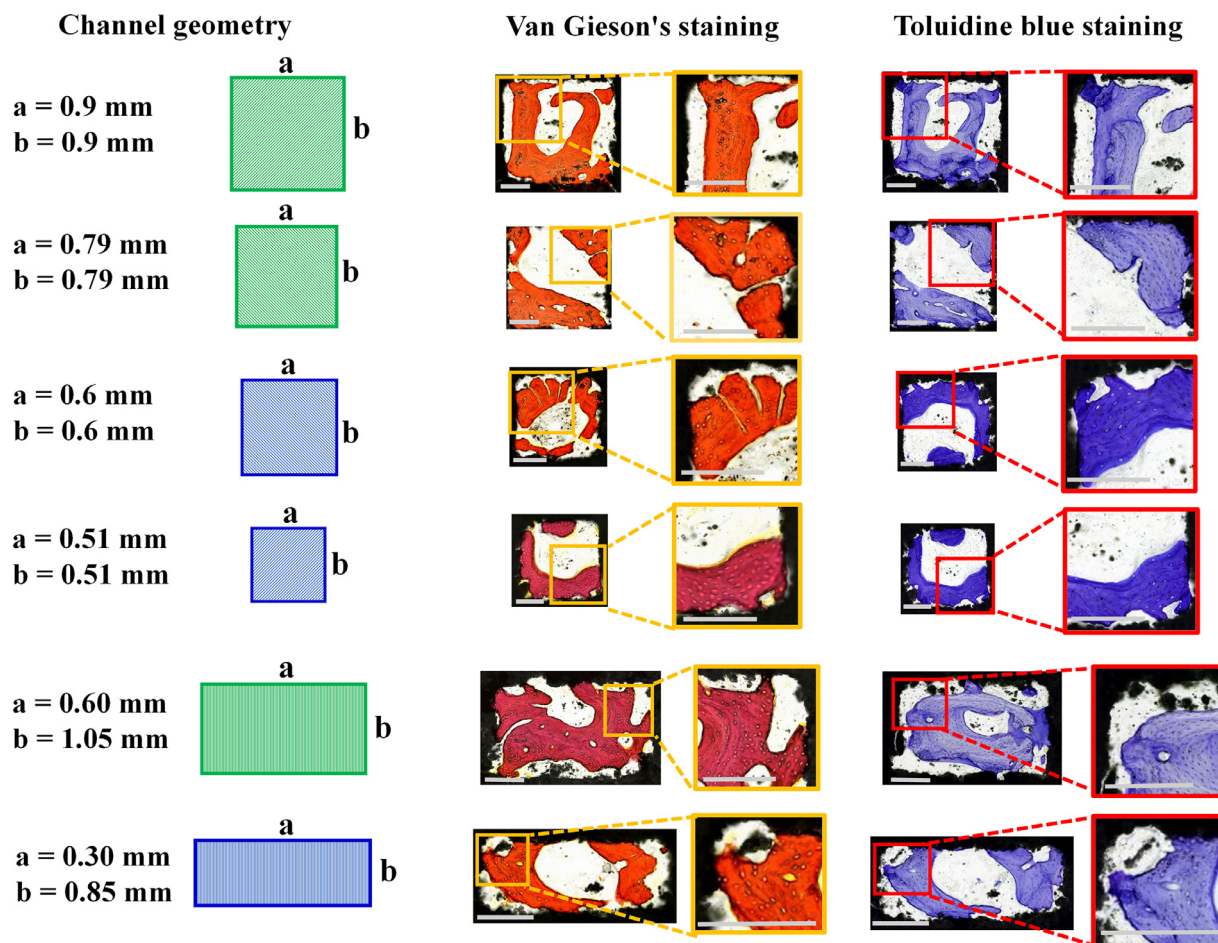


Fig. 6. Representative histological results of isolated rectangular channels. The Toluidine Blue staining (black: implant; blue: bone) and Van Gieson's staining (black: implant; red: bone) were used to quantify the newly formed bone in channels at cross-sections located approximately in the middle of the scaffolds and ran parallel to their top and bottom surfaces. Scale bar = 0.25 mm.

mean curvature) and convex (positive mean curvature) surfaces as depicted in Fig. 8. The scaffold was a cylinder with a diameter and a height of 7 mm and 3.2 mm, respectively. Inside, there was a hollow cubic cavity with sides of 4 mm. One side of the cubic cavity was flat (zero mean curvature) while the other sides of the cube featured four curved surfaces, consisting of concave and convex curvatures with different diameters of 0.3 mm, 0.6 mm, and 0.9 mm. Of the four samples implanted in rabbits, one broke post-implantation, and two were lost due to the death of the animal.

Fig. 9 illustrates the bone formation results at two different cross-sections cut approximately at the middle of the unbroken sample. The histological image of the broken implant is provided in the Supplementary materials. As depicted in Fig. 9, the formation of new bone tissue was prominently observed on the concave surfaces (regions with negative mean curvature II, IV, VIII, X, XIV, and XVI). In contrast, flat surfaces (regions with zero mean curvature XII) and those with a convex shape (regions with positive mean curvature IX, XI, XIII, XV, and VI), especially those with larger radii, exhibited minimal to no osteogenesis. Notably, significant bone formation was also observed on the corners (large local negative curvature) of the cubic cavity (*i.e.*, regions XVII, XIX, and XVIII).

These findings align with the results obtained from the histological analysis of the broken sample (Fig. S1 in Supplementary materials). Specifically, concave surfaces with diameters of 0.6 mm and 0.9 mm (regions VIII, X, XIV, and XVI) exhibited noticeably more significant osteogenesis compared to convex surfaces with similar diameters (regions IX, XI, XIII, and XV).

4. Discussion

Porous synthetic scaffolds are central to bone tissue engineering strategies because they provide the necessary 3-D framework for bone tissue ingrowth. The clinical success of these scaffolds depends not only on the intrinsic properties of their constitutive material but also on their internal macroscopic geometry [32]. The internal geometric features of tissue scaffolds, particularly pore size, shape, and curvature, have been shown to significantly influence the kinetics of tissue deposition. Hence, understanding the precise role of these geometric factors is critical for design and fabrication of effective scaffolds for bone tissue engineering. Although previous studies have imparted significant insights into how various geometric features of scaffolds may modulate bone tissue formation [28], they have not often isolated the specific effects of pore size, shape, and curvature, especially *in vivo* settings, from other contributory osteogenic parameters.

Control over the internal pore geometry of scaffolds is highly dependent on the capability of the fabrication technique [33]. While various conventional manufacturing approaches, such as the sponge template method, solvent casting, and gas foaming are utilized for scaffold preparation, they possess limitations [34]. A primary limitation is their inability to precisely control the geometry and distribution of the pores within the scaffolds. Recent advances in 3D printing technique allow for the creation of scaffolds with precise dimensions and a well-structured internal architecture essential for enhanced bone regeneration.

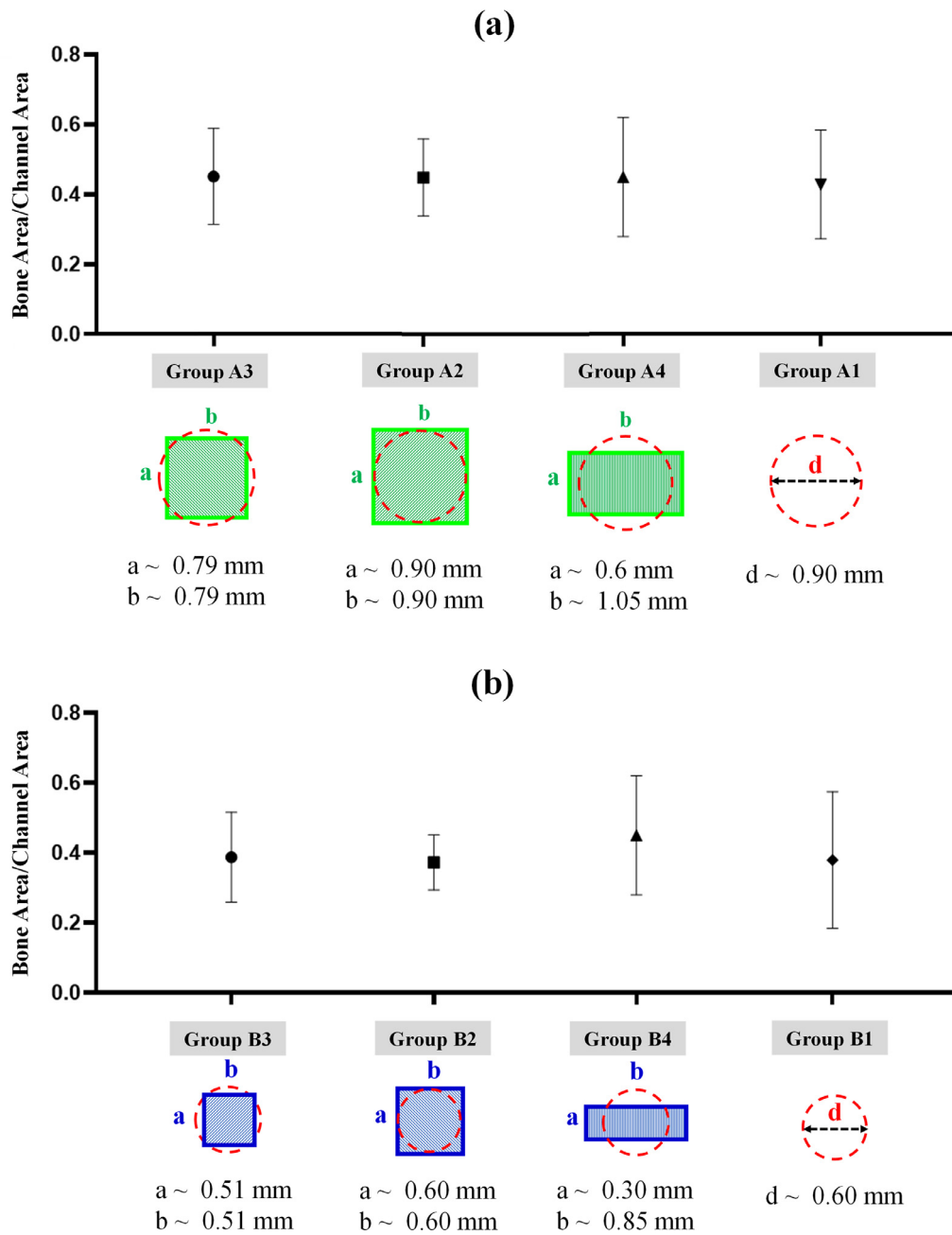


Fig. 7. Quantitative bone formation results of isolated rectangular channels. The ratios of the new bone area to the total channel area were measured at histological cross-sections (Van Gieson's staining) located in the middle of samples and running parallel to their top and bottom surfaces. (a) A comparison was made between three rectangular channels with dimensions of 0.79 mm \times 0.79 mm ($n = 8$), 0.90 mm \times 0.90 mm ($n = 8$), 0.60 mm \times 1.05 mm ($n = 8$), and their corresponding circular channel with a diameter of 0.9 mm ($n = 8$); (b) A comparison was made between three rectangular channels with dimensions of 0.51 mm \times 0.51 mm ($n = 7$), 0.60 mm \times 0.60 mm ($n = 7$), 0.3 mm \times 0.85 mm ($n = 10$), and their corresponding circular channel with a diameter of 0.6 mm ($n = 8$).

In the present study, utilizing our recently developed 3D printing technology [28], we were able to efficiently fabricate complex 3D printed bioceramic scaffolds having different channel sizes, shapes, and curvatures and systematically investigated their exclusive impact on *in vivo* bone tissue regeneration.

Pore size has been known to significantly affect bone tissue formation. We previously demonstrated that increasing the pore size from ~ 0.4 mm to ~ 0.6 mm could substantially increase bone ingrowth in 3D scaffolds implanted in rabbit calvarial defects [17]. Cheng et al. [35], demonstrated that magnesium scaffolds with two pore sizes of 0.25 mm and 0.4 mm, exhibited enhanced bone formation in the larger pore, due to the newly formed blood vessels

which supply sufficient oxygen and nutrients for osteoblastic activity. In the present study, we utilized 3D printing to fabricate scaffolds with isolated channel sizes of 0.3 mm, 0.6 mm, 0.9 mm, 1.2 mm, and 1.5 mm to systematically explore the exclusive impact of channel size in osteogenesis *in vivo*.

Histological analysis at 8 weeks indicated that the circular channels with diameters of approximately 0.9 mm facilitated significantly greater bone tissue formation than those with diameters of 0.3 mm and 1.5 mm (Fig. 3). Notably, there was no marked difference in bone formation, defined as the ratio of bone tissue area formed within a channel to the total channel area, between channels with diameters of 0.6 mm, 0.9 mm, and 1.2 mm.

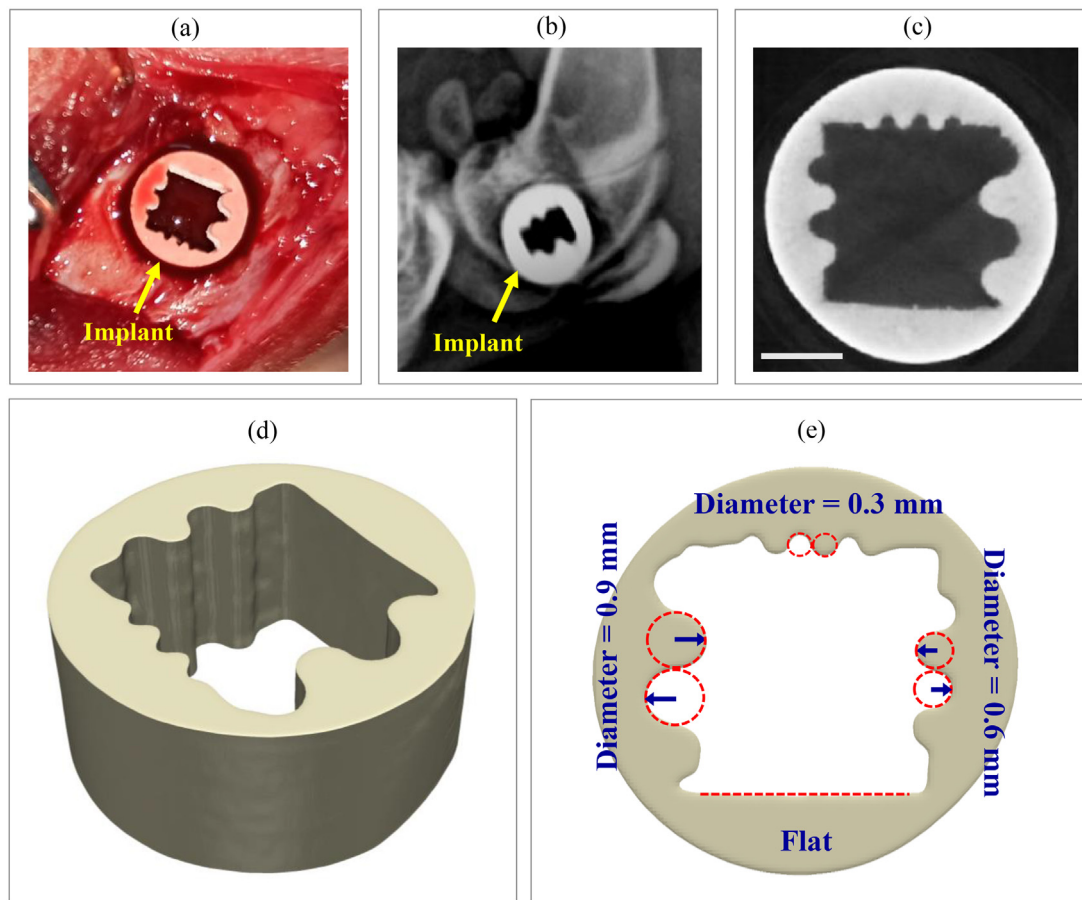


Fig. 8. Geometric and surgical details of scaffolds featuring flat, convex, and concave surfaces. (a) an image showing the implantation site in a rabbit femur; (b) a post-operative x-ray image of the surgical site; (c) a cross-sectional μ -CT image of the implant. This cross-section is perpendicular to the longitudinal direction of the channels; (d) a 3D reconstructed μ -CT scan of the implant (e) a cross-section of the 3D reconstructed implant depicting concave and convex surfaces with 0.3 mm, 0.6 mm, and 0.9 mm curvature diameter. Scale bar = 2 mm.

This observation is in alignment with the findings of the *in vivo* study conducted by Ghayor et al. [36] which revealed that the ideal pore/bottleneck dimension for bone substitutes falls within the range of 0.7–1.2 mm.

Channels can exhibit various shapes, from rounded configurations (e.g., circular) to those with distinct sharp corners (i.e., rectangular). In this study, we further investigated the effects of these distinct channel shapes, comparing sharp-cornered channels with rounded, circular ones. Our results demonstrated no significant difference in bone tissue formation between circular and rectangular channels in channels size range between 0.6 mm and 0.9 mm. Additionally, rectangular channels with aspect ratios exceeding one, had comparable bone tissue growth volume, to channels with a square aspect ratio. This suggests that modifying the width or height of a rectangular channel, while maintaining its total surface area, does not influence the bone tissue formation outcome within the channel.

Previous studies have suggested that pore curvature might be a significant determinant of osteogenesis in tissue scaffolds. Cells within the tissue are known to detect and respond to radii of curvature significantly larger than their own size [37]. An *in vivo* study by U. Ripamonti et al. [38] was one of the first to reveal the critical role of concavity in initiating the induction of bone formation. Furthermore, Paris et al. [39] showed that a 3D scaffold with both concave and convex surfaces promoted enhanced bone formation on its concave surfaces *in vivo*. However, their study did not maintain consistent mean curvature diameters between these surfaces,

leaving the systematic effects of convexity and concavity on bone tissue formation unexplored.

The current *in vivo* study presented a systematic approach to investigate the effects of surface curvature on bone tissue formation. We utilized stereo-lithography (SLA) 3D printing technique to fabricate ceramic scaffolds that feature a large cubic cavity. On the sides of this cavity, we created both concave and convex surfaces with consistent curvature diameters. These surfaces had varying diameters of 0.3 mm, 0.6 mm, and 0.9 mm. By focusing on this specific design, we aimed to exclude the influences of other osteogenic parameters porosity, channel size, interconnectivity, permeability, material composition, degradation rate, and surface roughness; all known to impact bone tissue regeneration [7–10,40].

As illustrated in Fig. 9, the volume of new bone tissue varied with the sign of curvature (i.e., positive or negative mean curvature). Evidently, concave surfaces exhibited greater tissue deposition, in comparison to both convex and flat surfaces. The bone formation surface area measured from the histological sections indicated that the average bone formation on concave surfaces was greater than that on convex surfaces. It was approximately 1.7, 2.3, and 3.5 times higher in concave surfaces with diameters of 0.3 mm, 0.6 mm, and 0.9 mm, respectively, compared with convex surfaces. Such patterns of bone tissue formation validate the curvature-driven effects previously suggested by numerical simulations conducted on bone tissue scaffolds [41]. Additionally, significant bone formation was observed on the corners of the cubic

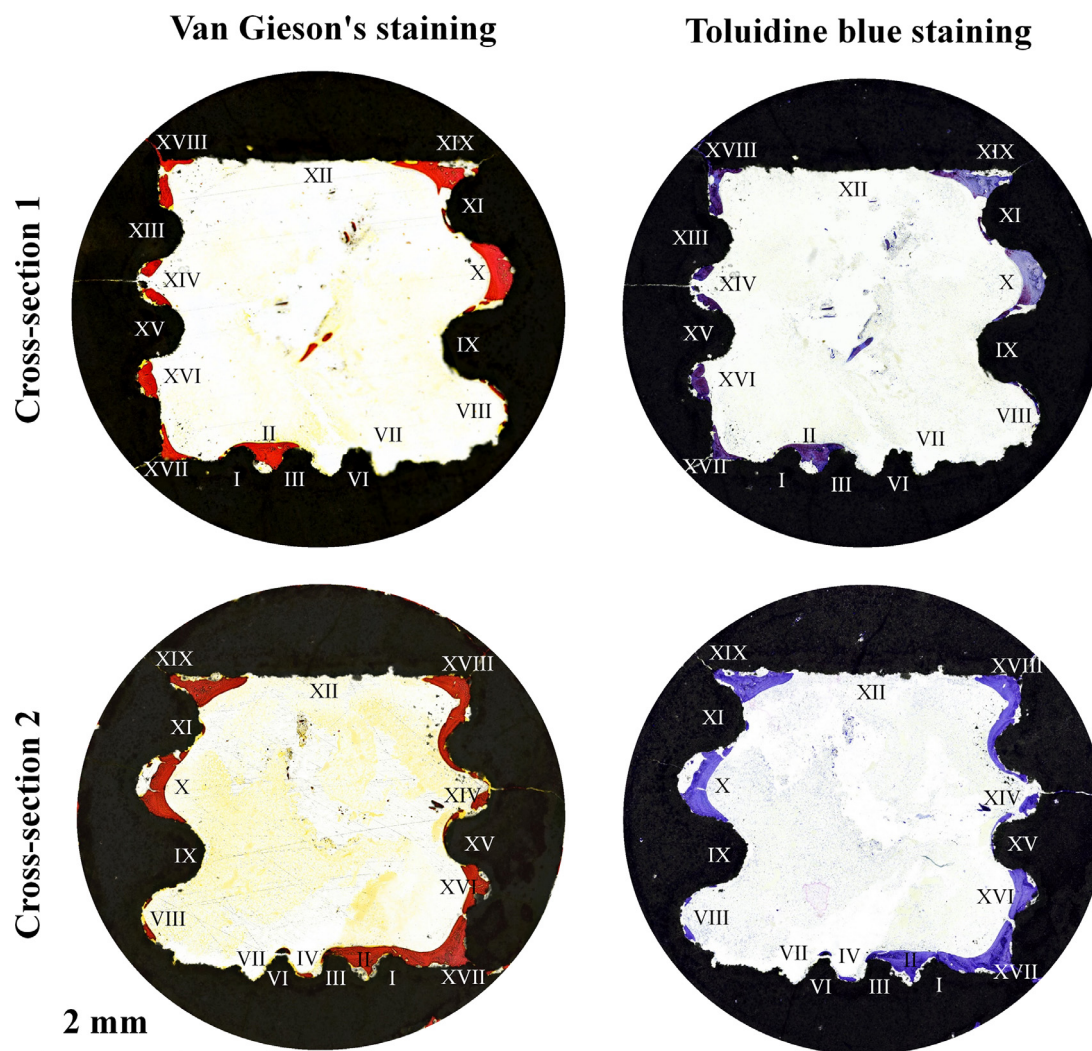


Fig. 9. Histological results of the scaffold featuring concave and convex surfaces. The Toluidine Blue staining (black: implant; blue: bone) and Van Gieson's staining (black: implant; red: bone) were used to quantify the newly formed bone in implants at two different cross-sections located roughly in the middle of the implant.

cavity, indicating sharp corners (large negative mean curvatures) could favor osteogenesis.

Our research focused on bone tissue formation within isolated channels, necessitating further studies to determine how these insights might translate to the design of three-dimensional scaffolds with intricate, interconnected pore networks. For example, P. Yilgor et al. [42] studied the impact of three-dimensional scaffold architecture on the healing of bone defects, demonstrating that open, accessible pore geometry and large pore surface area enhanced bone regeneration. Furthermore, gradient and hierarchical scaffolds have shown promise in enhancing bone tissue formation outcomes [43,44]. Such architectures can more accurately replicate the natural bone hierarchy from macro to nanoscales, facilitating the in-growth of bone and the formation of vascular networks.

Although this study investigated the effects of various geometric properties of bone tissue scaffolds *in vivo*, limitations exist. To systematically investigate the effects of curvature, we printed curved channels on the walls of a relatively large cubic cavity inside the scaffolds. Although this approach allows for the systematic investigation of surface concavity in a 2D setting, it falls short of replicating the three-dimensional complexity of actual scaffolds. Furthermore, while this study offered systematic insights into the influence of pore architecture on bone tissue formation, it did not examine other vital parameters such as scaffold material proper-

ties, surface characteristics, and biophysical stimuli, as these were outside the study's defined scope.

5. Conclusion

The findings of this study provide a systematic investigation of scaffold macroscopic geometry, paving the way for the rational design of more effective bone tissue scaffolds. Notably, we conducted a focused examination of the role of pore size in osteogenesis. Our results suggest that pore sizes in the range of 0.6–1.2 mm could enhance bone tissue formation. Furthermore, we demonstrated that circular and square shaped pores exhibited similar bone tissue formation. Additionally, the present study systematically demonstrated the favorable influence of negative curvature (concave surfaces and sharp corners) on bone tissue formation *in vivo*. Nevertheless, the present study concentrated on surfaces exhibiting zero Gaussian curvature, implying they were curved in one direction while being flat in the orthogonal direction. As a result, there is an avenue for future research to investigate the effects of surfaces with non-zero Gaussian curvatures on *in vivo* bone formation. Furthermore, a deeper exploration into the time-dependent dynamics of bone tissue formation might be a valuable avenue for future research, especially by incorporating more time points throughout the study.

Declaration of competing interest

The authors declare that they have no known competing financial interests or personal relationships that could have appeared to influence the work reported in this paper.

CRediT authorship contribution statement

Ali Entezari: Conceptualization, Data curation, Formal analysis, Investigation, Methodology, Software, Validation, Writing – original draft, Writing – review & editing. **Qianju Wu:** Conceptualization, Formal analysis, Methodology, Resources, Validation, Writing – original draft, Writing – review & editing. **Mohammad Mirkhalaf:** Conceptualization, Methodology, Resources, Writing – review & editing. **Zufu Lu:** Formal analysis, Investigation, Resources, Writing – review & editing. **Iman Roohani:** Formal analysis, Investigation, Validation, Conceptualization, Writing – review & editing. **Qing Li:** Formal analysis, Investigation, Methodology, Software, Writing – review & editing. **Colin R. Dunstan:** Conceptualization, Formal analysis, Validation, Writing – original draft. **Xinquan Jiang:** Conceptualization, Project administration, Resources, Supervision, Writing – original draft, Writing – review & editing. **Hala Zreiqat:** Conceptualization, Formal analysis, Funding acquisition, Investigation, Methodology, Project administration, Supervision, Writing – original draft, Writing – review & editing.

Acknowledgments

A. Entezari and Q. Wu contributed equally to this work. We acknowledge the Sydney Microscopy & Microanalysis facility at the University of Sydney.

Funding information

This work was supported by a grant from Australian National Health and Medical Research Council (NHMRC).

Supplementary materials

Supplementary material associated with this article can be found, in the online version, at [doi:10.1016/j.actbio.2024.04.020](https://doi.org/10.1016/j.actbio.2024.04.020).

References

- [1] A.S. Greenwald, S.D. Boden, V.M. Goldberg, Y. Khan, C.T. Laurencin, R.N. Rosier, Bone-graft substitutes: facts, fictions, and applications, *J. Bone Joint Surg. Am.* 83-A Suppl 2 Pt 2 (2001) 98–103.
- [2] H.S. Sohn, J.K. Oh, Review of bone graft and bone substitutes with an emphasis on fracture surgeries, *Biomater. Res.* 23 (2019) 9.
- [3] M. Alonzo, F.A. Primo, S.A. Kumar, J.A. Mudloff, E. Dominguez, G. Fregoso, N. Ortiz, W.M. Weiss, B. Joddar, Bone tissue engineering techniques, advances, and scaffolds for treatment of bone defects, *Curr. Opin. Biomed. Eng.* 17 (2021) 100248.
- [4] H. Qu, H. Fu, Z. Han, Y. Sun, Biomaterials for bone tissue engineering scaffolds: a review, *RSC Adv.* 9 (45) (2019) 26252–26262.
- [5] K. Lin, R. Sheikh, S. Romanazzo, I. Roohani, 3D printing of bioceramic scaffolds—barriers to the clinical translation: from promise to reality, and future perspectives, *Materials (Basel, Switzerland)* 12 (17) (2019).
- [6] L. Roseti, V. Parisi, M. Petretta, C. Cavallo, G. Desando, I. Bartolotti, B. Grigolo, Scaffolds for bone tissue engineering: state of the art and new perspectives, *Mater. Sci. Eng.: C* 78 (2017) 1246–1262.
- [7] V. Karageorgiou, D. Kaplan, Porosity of 3D biomaterial scaffolds and osteogenesis, *Biomaterials* 26 (27) (2005) 5474–5491.
- [8] J.J. Li, M. Ebied, J. Xu, H. Zreiqat, Current approaches to bone tissue engineering: the interface between biology and engineering, *7(6)* (2018) 1701061.
- [9] A. Entezari, M.V. Swain, J.J. Gooding, I. Roohani, Q. Li, A modular design strategy to integrate mechanotransduction concepts in scaffold-based bone tissue engineering, *Acta Biomater.* 118 (2020) 100–112.
- [10] S.J.P. Callens, R.J.C. Uyttendaele, L.E. Fratila-Apachitei, A.A. Zadpoor, Substrate curvature as a cue to guide spatiotemporal cell and tissue organization, *Biomaterials* 232 (2020) 119739.
- [11] V. Karageorgiou, D. Kaplan, Porosity of 3D biomaterial scaffolds and osteogenesis, *Biomaterials* 26 (27) (2005) 5474–5491.
- [12] S. Bose, M. Roy, A. Bandyopadhyay, Recent advances in bone tissue engineering scaffolds, *30(10)* (2012) 546–554.
- [13] S.D. Puckett, E. Taylor, T. Raimondo, T.J. Webster, The relationship between the nanostructure of titanium surfaces and bacterial attachment, *Biomaterials* 31 (4) (2010) 706–713.
- [14] S. Ehrig, B. Schamberger, C.M. Bidan, A. West, C. Jacobi, K. Lam, P. Kollmannsberger, A. Petersen, P. Tomancak, K. Kommareddy, F.D. Fischer, P. Fratzl, J.W.C. Dunlop, Surface tension determines tissue shape and growth kinetics, *5(9)* (2019) eaav9394.
- [15] Y. Tian, H. Ma, X. Yu, B. Feng, Z. Yang, W. Zhang, C. Wu, Biological response of 3D-printed β -tricalcium phosphate bioceramic scaffolds with the hollow tube structure, *Biomed. Mater.* 18 (3) (2023) 034102.
- [16] M. Zhang, R. Lin, X. Wang, J. Xue, C. Deng, C. Feng, H. Zhuang, J. Ma, C. Qin, L. Wan, J. Chang, C. Wu, 3D printing of Haversian bone-mimicking scaffolds for multicellular delivery in bone regeneration, *Sci. Adv.* 6 (12) (2020) eaaz6725.
- [17] A. Entezari, I. Roohani, G. Li, C.R. Dunstan, P. Rognon, Q. Li, X. Jiang, H. Zreiqat, Architectural design of 3D printed scaffolds controls the volume and functionality of newly formed bone, *8(1)* (2019) 1801353.
- [18] Influence of geometry and architecture on the in vivo success of 3D-printed scaffolds for spinal fusion, *27(1–2)* (2021) 26–36.
- [19] P.R. Buenzi, M. Lanaro, C.S. Wong, M.P. McLaughlin, M.C. Allenby, M.A. Woodruff, M.J. Simpson, Cell proliferation and migration explain pore bridging dynamics in 3D printed scaffolds of different pore size, *Acta Biomater.* 114 (2020) 285–295.
- [20] M. Mastrogiacomo, S. Scaglione, R. Martinetti, L. Dolcini, F. Beltrame, R. Cancedda, R. Quarto, Role of scaffold internal structure on *in vivo* bone formation in macroporous calcium phosphate bioceramics, *Biomaterials* 27 (17) (2006) 3230–3237.
- [21] J. Konka, J. Buxadera-Palomero, M. Espanol, M.-P. Ginebra, 3D printing of hierarchical porous biomimetic hydroxyapatite scaffolds: adding concavities to the convex filaments, *Acta Biomater.* 134 (2021) 744–759.
- [22] V. Karageorgiou, D.J.B. Kaplan, Porosity of 3D biomaterial scaffolds and osteogenesis, *26(27)* (2005) 5474–5491.
- [23] C.M. Bidan, K.P. Kommareddy, M. Rumpler, P. Kollmannsberger, P. Fratzl, J.W. Dunlop, Geometry as a factor for tissue growth: towards shape optimization of tissue engineering scaffolds, *Adv. Healthc. Mater.* 2 (1) (2013) 186–194.
- [24] F.S.L. Bobbert, A.A. Zadpoor, Effects of bone substitute architecture and surface properties on cell response, angiogenesis, and structure of new bone, *J. Mater. Chem. B* 5 (31) (2017) 6175–6192.
- [25] S.J.P. Callens, D. Fan, I.A.J. van Hengel, M. Minneboo, P.J. Díaz-Payno, M.M. Stevens, L.E. Fratila-Apachitei, A.A. Zadpoor, Emergent collective organization of bone cells in complex curvature fields, *Nat. Commun.* 14 (1) (2023) 855.
- [26] D.J. Lee, J. Kwon, Y.I. Kim, X. Wang, T.J. Wu, Y.T. Lee, S. Kim, P. Miguez, C.C. Ko, Effect of pore size in bone regeneration using polydopamine-laced hydroxyapatite collagen calcium silicate scaffolds fabricated by 3D mould printing technology, *Orthod. Craniofac. Res.* 22 Suppl 1 (Suppl 1) (2019) 127–133.
- [27] F. Deng, L. Liu, Z. Li, J. Liu, 3D printed Ti6Al4V bone scaffolds with different pore structure effects on bone ingrowth, *J. Biol. Eng.* 15 (1) (2021) 4.
- [28] M. Mirkhalaf, X. Wang, A. Entezari, C.R. Dunstan, X. Jiang, H. Zreiqat, Redefining architectural effects in 3D printed scaffolds through rational design for optimal bone tissue regeneration, *Appl. Mater. Today* 25 (2021) 101168.
- [29] M. Mirkhalaf, J. Goldsmith, J. Ren, A. Dao, P. Newman, A. Schindeler, M.A. Woodruff, C.R. Dunstan, H. Zreiqat, Highly substituted calcium silicates 3D printed with complex architectures to produce stiff, strong and bioactive scaffolds for bone regeneration, *Appl. Mater. Today* 25 (2021) 101230.
- [30] Y. Jin, W. Zhang, Y. Liu, M. Zhang, L. Xu, Q. Wu, X. Zhang, Z. Zhu, Q. Huang, X. Jiang, rhPDGF-BB via ERK pathway osteogenesis and adipogenesis balancing in ADCs for critical-sized calvarial defect repair, *Tissue Eng. Part A* 20 (23–24) (2014) 3303–3313.
- [31] A. Scarano, A. Piattelli, V. Perrotti, L. Manzon, G. Iezzi, Maxillary sinus augmentation in humans using cortical porcine bone: a histological and histomorphometrical evaluation after 4 and 6 months, *Clin. Implant Dent. Relat. Res.* 13 (1) (2011) 13–18.
- [32] M.N. Collins, G. Ren, K. Young, S. Pina, R.L. Reis, J.M. Oliveira, Scaffold fabrication technologies and structure/function properties in bone tissue engineering, *31(21)* (2021) 2010609.
- [33] C. Lim, K.S. Chian, K.F. Leong, Development of cryogenic prototyping for tissue engineering, *Virtual Phys. Prototyp.* 3 (2008) 25.
- [34] D.W. Hutmacher, Scaffold design and fabrication technologies for engineering tissues – State of the art and future perspectives, *J. Biomater. Sci., Polym. Edit.* 12 (1) (2001) 107–124.
- [35] M.Q. Cheng, T. Wahafu, G.F. Jiang, W. Liu, Y.Q. Qiao, X.C. Peng, T. Cheng, X.L. Zhang, G. He, X.Y. Liu, A novel open-porous magnesium scaffold with controllable microstructures and properties for bone regeneration, *Sci. Rep.* 6 (2016) 24134.
- [36] C. Ghayor, F. Weber, Osteoconductive microarchitecture of bone substitutes for bone regeneration revisited, *9* (2018) 388969.
- [37] X. Lin, S. Romanazzo, K. Lin, C. Kelly, J.J. Gooding, I. Roohani, Elliptical supracellular topographies regulate stem cells migratory pattern and osteogenic differentiation, *Materialia* 14 (2020) 100870.
- [38] U. Ripamonti, *The Geometric Induction of Bone Formation*, CRC Press, 2020.
- [39] M. Paris, A. Götz, I. Hettrich, C.M. Bidan, J.W.C. Dunlop, H. Razi, I. Zizak, D.W. Hutmacher, P. Fratzl, G.N. Duda, W. Wagermaier, A. Cipitria, Scaffold cur-

- vature-mediated novel biomineralization process originates a continuous soft tissue-to-bone interface, *Acta Biomater.* 60 (2017) 64–80.
- [40] A.G. Mitsak, J.M. Kemppainen, M.T. Harris, S.J. Hollister, Effect of polycaprolactone scaffold permeability on bone regeneration *in vivo*, *Tissue Eng. Part A* 17 (13–14) (2011) 1831–1839.
- [41] S. Ehrig, B. Schamberger, C.M. Bidan, A. West, C. Jacobi, K. Lam, P. Kollmannsberger, A. Petersen, P. Tomancak, K. Kommareddy, Surface tension determines tissue shape and growth kinetics, 5(9) (2019) eaav9394.
- [42] P. Yilgor, G. Yilmaz, M.B. Onal, I. Solmaz, S. Gundogdu, S. Keskil, R.A. Sousa, R.L. Reis, N. Hasirci, V. Hasirci, An *in vivo* study on the effect of scaffold geometry and growth factor release on the healing of bone defects, *J. Tissue Eng. Regen. Med.* 7 (9) (2013) 687–696.
- [43] A. Alshammari, F. Alabdah, W. Wang, G. Cooper, Virtual design of 3D-printed bone tissue engineered scaffold shape using mechanobiological modeling: relationship of scaffold pore architecture to bone tissue formation, 15(19) (2023) 3918.
- [44] J.R. Jones, S. Lin, S. Yue, P.D. Lee, J.V. Hanna, M.E. Smith, R.J. Newport, Bioactive glass scaffolds for bone regeneration and their hierarchical characterisation, *Proc. Inst. Mech. Eng. Part H, J. Eng. Med.* 224 (12) (2010) 1373–1387.